Performance Prediction, Sensitivity Analysis and Parametric Optimization of Electrical Impedance Tomography Using A Bioelectrical Tissue Simulation Platform

Mingde Zheng, *Member, IEEE,* Bassem Ibrahim, *Student Member, IEEE*

Abstract— There is an urgent need to bring forth portable, low-cost, point-of-care diagnostic instruments to monitor patient health and wellbeing. This is elevated by the COVID-19 global pandemic in which the availability of proper lung imaging equipment has proven to be pivotal in the timely treatment of patients. Electrical impedance tomography (EIT) has long been studied and utilized as such a critical imaging device in hospitals especially for lung ventilation. Despite decades of research and development, many challenges remain with EIT in terms of 1) optimal image reconstruction algorithms, 2) simulation and measurement protocols, 3) hardware imperfections, and 4) uncompensated tissue bioelectrical physiology. Due to the inter-connectivity of these challenges, singular solutions to improve EIT performance continue to fall short of the desired sensitivity and accuracy. Motivated to gain a better understanding and optimization of the EIT system, we report the development of a bioelectric facsimile simulator demonstrating the dynamic operations, sensitivity analysis, and reconstruction outcome prediction of the EIT sensor with stepwise visualization. By building a sandbox platform to incorporate full anatomical and bioelectrical properties of the tissue under study into the simulation, we created a tissue-mimicking phantom with adjustable EIT parameters to interpret bioelectrical interactions and to optimize image reconstruction accuracy through improved hardware setup and sensing protocol selections.

Keywords— Electrical impedance tomography; bioelectrical phantom; simulation; image reconstruction; parametric optimization, sensitivity and selectivity analysis.

I. INTRODUCTION

At the wake of the COVID-19 global pandemic, it has become increasingly clear that the lack of readily deployable, portable, low-cost, point-of-care diagnostic and imaging instrument can significantly hinder the prompt diagnosis and treatment of affected patients. Conventionally, pulse oximetry is widely utilized as the palliative care option to indirectly check patient ventilation health in resource-limited setting, however the use of this device has been cautioned due to the fluctuating accuracy from motion artifacts, device-to-device variations, existing patient medical conditions (e.g. poor peripheral perfusion) [1]. Most importantly, respiratory functions of the lungs are critical organs being affected by COVID-19 viruses and must be the center of care and continuous monitoring. It is thereby imperative to have the proper imaging instruments readily available to track patient respiratory health. Electrical impedance tomography (EIT) [2] sensor is a highly promising imaging modality that is cost-effective, easy-to-operate and a potentially personalizable, wearable sensor, making it particularly useful in overcrowded hospital setting and resource-constrained healthcare environments.

Historically, EIT has played a significant role in the clinical domain from monitoring physiological functions to diagnosing various diseases. Attributed to its unique ability in interacting with the dielectric properties of the human tissues to provide imaging contrast, EIT is a radiation-free imaging modality unlike its X-ray tomography counterpart. It's non-invasive, cost-effective, and has relatively smaller technology footprint compared to other medical imaging modalities. EIT has found favor in numerous medical imaging applications such as cranial imaging in newborns [3], lung monitoring [4]–[6], hyperthermia treatment [7], pediatric lung disease diagnosis [8], breast imaging [9], brain imaging [10]. Its applicability has also been found in biotechnology sector to aid in cell culture studies and monitoring [11], [12] as well as In-Vitro Diagnostics or Lab-on-Chip system development for single cell and biochemical pathway analysis [12].

EIT operates on the principle of electrical conductivity contrast in the body. By injecting a non-perceptible, constant, sinusoidal current to a subject through surface electrodes, the boundary potentials are measured to reconstitute the resistivity distribution within the subject volume by using an optimal image reconstruction algorithm. Briefly, a ring of circumferential electrodes as few as 4 but up to 32 are commonly used to measure these potential voltages. There are many unique stimulation and measurement protocols available that aim to increase data volume [13] or content diversity via multi-frequency EIT [14]. Substantial efforts are made in EIT hardware improvement over the past few decades [14]–[16], however, desirable quality of image reconstruction remains to be challenging. The difficulties arise from having to solve an inverse problem in which it is non-linear, ill-conditioned and ill-posed in nature [17]. Because electric current tends to propagate volumetrically within a body and distribute non-linearly, thus large variations in the body's resistivity may only produce a small change in the surface measurements, and vice versa is also a challenge. For these reasons, high sensitivity has been difficult to achieve with increasing tissue depth. This is often made worse with effects such as: 1) imperfections in the electronic hardware and improper electrode contacts with the skin; 2) non-optimal measurement and stimulation protocols; 3) 2D algorithmic calculation rather than 3D; 4) non-standard

M.Z. is a senior scientist with the Nokia Bell Labs at New Providence, NJ 07974 USA (corresponding author contact: 908-679-5917; e-mail: Mingde.zheng@nokia-bell-labs.com).

B.I. was a visiting researcher with the Nokia Bell Labs at New Providence, NJ 07974 USA (e-mail: bassem.zaki@gmail.com).

anatomical and physiological models for tissue under analysis [18].

Image reconstruction of EIT is commonly performed using EIDOR (an open source Electrical Impedance and Diffused Optical Reconstruction Software) [19]. Its finite element model approach has been the norm for decades to generate mesh networks, calculate the forward problem and solve the inverse problem via customizable library of generic algorithms [20]. Although it has been the go-to platform for exploring and implementing novel algorithms and parametric tryouts, there are many desirable features that are missing which would better aid in the improved understanding and implementation of EIT sensors for the target applications.

In this paper, we introduce an alternative simulation platform that is based on the cell equivalent electrical circuit model of human tissues to simulate the biological phantom of interest. By building the phantom "cell-by-cell", in which the phantom consists of interconnected circuits to represent each cell type, and collectively forming tissues and ultimately the physical attributes and properties of interest, we demonstrate that this bioelectric representation provides a more accurate response prediction from EIT sensor interrogation. By integrating MATLAB's analytical engine with SPICE's simulator, we formulated novel processes to evaluate EIT's sensitivity and selectivity on a simplified phantom. We demonstrate a new simulation tool capable of realizing the following features even beyond EIT and applicable to any bioelectrical sensors.

1) Modeling simple and complex dynamic physiological processes over time from pulsatile movements of blood vessels to transient motions of heart, or the lungs.

2) Optimize EIT sensor for the appropriate biological targets through hardware and operation protocol adjustments based on bioelectrical response feedback from tissue model.

3) Sensor detection sensitivity and selectivity visual maps showing specific regions of sensing strengths and vulnerabilities.

4) More accurate prediction of imaging resolutions, limit of detection and reconstruction outcome that matches real-life measurements using our tissue model circuits.

5) Customizable phantom features with tunable physical, and bioelectrical properties and degrees of complexity to accommodate/simulate for specific biological relevance.

6) Visualization of the operation process in which both stimulation current and voltage distribution are shown dynamically with the phantom.

In section II of this paper, the methods to implement the bioelectrical phantom, simulation platform, sensitivity and selectivity analysis are explained. Simulation performance is also evaluated through selected experiments on two key EIT parameters in this section. Section III covers the reporting and discussion of the simulation's performance outcomes. The conclusion and outlook are presented in section IV.

II. METHODS

The success of EIT as a biological imaging device comes from the intrinsic electrical properties of cells and tissues. Since the unique composition of each cell type renders unique dielectric responses (e.g. impedance magnitude and phase) upon electrical current stimulation, we thus take a circuit analysis approach to evaluate the collective responses of the resultant tissue-equivalent circuits build from networks of single cells. In this work, we chose a cross-sectional geometry of a human upper arm with major tissue constituents or features in simplified shapes and sizes as a demonstration of proof-of-concept. Precise anatomical geometry can be fine-adjusted and populated by our algorithm at the expense of simulation time. A circumferential electrode arrangement on the surface of the phantom in even numbers was chosen with a 4-point Kelvin configuration for measurement and stimulation. At any given time, a set of two electrodes inject prescribed current while another prescribed set of two differential electrodes measure the voltages.
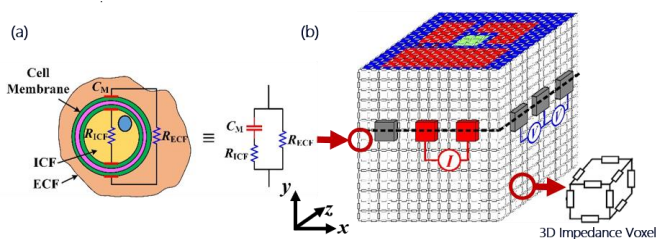

Figure 1. (a) Simplified cell equivalent circuit. (b) 3D phantom grid with four types of tissue features where each unit is an impedance voxel.

A. Bioelectrical Phantom

The fundamental constituent of the phantom was a simplified single cell equivalent circuit model consisting of an extracellular fluid resistor R_{ECF} in parallel with resistance from a membrane capacitor C_M in series with an intracellular fluid resistor R_{ICF} (Figure 1a). In the tissue space of the same cell type, this single bioelectrical cell was arranged and networked to form a local impedance grid in 2D or a voxel in 3D (Figure 1b). The dimension and shapes of these tissue-representing networks were constructed according to the boundary specifications in the MATLAB program. The values for these electrical elements were specific to each cell type, and they are widely reported in literature [21].

Four types of tissues were represented in our 3D phantom example of an upper arm cross-section (Figure 2a). As shown in Figure 2b, the subcutaneous fat tissue is shown in blue surrounding muscle tissues in red. Three shapes and sizes of muscles were configured to mimic their anatomical diversity in the body. In the core of the phantom is the bone tissue in green. Two arteries in maroon are positioned between muscles and fat, to highlight one of the smallest tissue types presented for detection. The composition of this phantom was customizable and automatically generated. They set the basis for determining the resolution, sensitivity and specificity of the EIT sensor in later section. A series of equidistant square electrodes were placed on the surface of the phantom with relatively defined size and position with respect to the 3D model. In our simulation, a total of 20 electrodes was chosen with 5 on each side of a 20 x 20 x 15 grid-size phantom. The

Arm Cross Section   Phantom Features

(a)

(b)

Muscles
0.3 mho/m
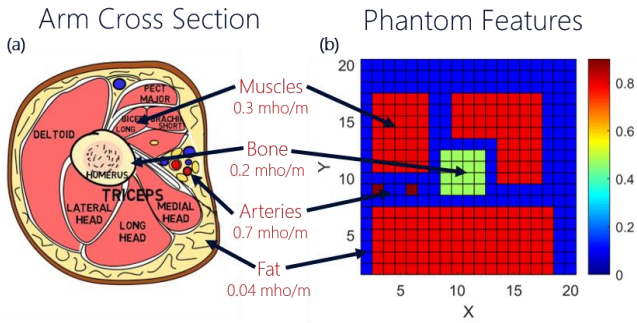
Bone
0.2 mho/m

Arteries
0.7 mho/m

Fat
0.04 mho/m

Figure 2. (a) 2D schematic of the upper arm cross section with major tissue constituents. (b) 2D plane view of the phantom with 4 types of simplified geometry of tissue. Intensity indicates conductivity in mho/m

default stimulation and measurement protocol follow that of the Neighboring method (Figure 3a), in which an adjacent electrode pair injected current while the other adjacent electrode pairs measured voltage in a rotational sequence until all remaining electrode pairs take a turn (Figure 3b). After which, the current injection electrode advanced to the next pair to begin the next frame of measurement. One round of completed current rotation can thus provide a total of 5100 measurements (20 current injections x 17 voltage readings x 15 planes). Another popular measurement configuration for comparison is the Opposite method, in which current is applied via opposite facing electrodes while voltages are measured by adjacent electrode pairs. An amplitude of 1 mA at 10 kHz frequency was used as the input for the stimulation. The selection of stimulation parameters influenced the analysis of responses between tissues, and thus vital in multi-frequency EIT implementations.
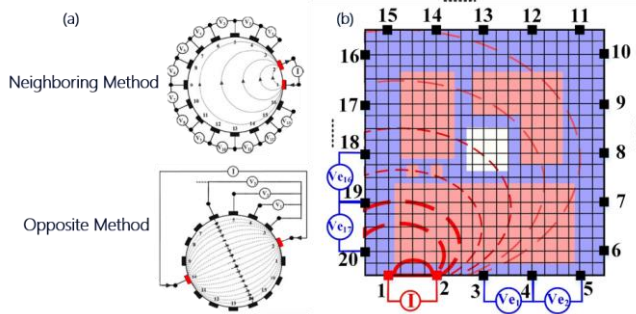

Figure 3. (a) Two stimulation and measurement protocols: the neighboring method and the opposite method. (b) The neighboring method is shown being applied with current schematically diffuse throughout the phantom feature in a 2D plane.

B. Simulation Platform

The simulation strategy was based on the Bio-Z impedance model realized using the MathWorks' MATLAB program and SPICE simulation toolkit developed previously [22]. Simulation input parameters such as phantom geometry, voxel conductivities, spatial arrangement of tissues and electrode, stimulating current amplitude, frequency and etc. were managed and initialized in the MATLAB program. MATLAB generates a circuit netlist that includes the connection between the resistors, capacitors, and electrical stimuli as specified by the 3D impedance model in each simulation. Subsequently LTSpice simulator from Analog Devices was invoked to perform the circuit simulations. The outcome is the calculation

of the dielectric responses of the phantom using the specified current source according to the input parameters. The resultant node voltage $V(x,y,z,f)$, current distribution $I(x,y,z,f)$ and grid impedance $Z(x,y,z,f)$ at the prescribed frequency in each 3D voxels were recorded and outputted in a multi-dimensional array for downstream calculation and analysis in MATLAB.

C. Sensitivity & Specificity Analysis

An impedance map of the 3D phantom was calculated from all constituting voxels in the grid network. In order to evaluate how sensitive the EIT sensor is to any impedance variation (e.g. as a result of user-defined anatomical deformation), we devised a sensitivity analysis process to computationally and graphically indicate regions of strongest and weakest changes for each frame of voltage measurements. In this study, we defined an impedance image $R(i,j,l)$ of the phantom based on the number of voxels N (20x20x15), and let i is an index in x-axis, j is an index in y-axis, l is an index in z-axis with i,j,l initial value of 1 increasing towards Ni,j =21 and Nl =15. We then defined a reference impedance image for each voxel having an arbitrary but equal impedance magnitude of 10 ohms, represented as

$$R(i,j,l)_{ref} = 10\Omega \; \forall \; i = 1{:}Ni, j = 1{:}Nj, l = 1{:}Nl.$$

The differential voltage measurement $Ve(k,s)$ from each pair of electrodes during an EIT operation is set up for current electrode pair k which ranges from 1 to all current injections of $Nelec$ =20 and s for voltage measurement which ranges from 1 to all voltage measurement of $Nelec - 3$=17. Thereby, a voltage vector $\overrightarrow{Ve}$ can be obtained to represent all stimulation measurement protocol as:

$$\overrightarrow{Ve} = \langle Ve(k,s) \;|_{k=1..Nelec,s=1..Nelec-3} \rangle = \langle Ve(1,1), ..., Ve(20,17) \rangle$$

For the sensitivity analysis of each voxel, we implemented a running operator that reduced the impedance value of an impedance map under test $R(i,j,l)_{n,m,p}$ one at a time to simulate a state of change for each frame of measurement comparing to the constant reference map $R(i,j,l)_{ref}$. This running comparison process provided an individual sensitivity map $\overline{\Delta Ve}_{k,s}(n,m,p)$ based on the subtractive voltage difference between the altered and constant reference having the form of:

$$\overline{\Delta Ve}_{k,s}(n,m,p) = Ve(k,s)_{n,m,p} - Ve(k,s)ref$$

$$\forall \; n = 1{:}Ni, m = 1{:}Nj, p = 1{:}Nl$$

$$\text{Where } R(i,j,l)_{n,m,p} = \begin{cases} 1\Omega & i = n, j = m, \; l = p \\ 10\Omega & i \neq n, j \neq m, \; l \neq p \end{cases}$$

Therefore, the individual sensitivity $\overline{\Delta Ve}_{k,s}(n,m,p)$ represents the voltage difference for current source k and voltage measurement s for any impedance changes at location (n,m,p). These were calculated then color-coded to visually demonstrate the effect of the impedance change of a voxel on the plotted electrode configuration.

Following a full cycle of the stimulation and measurement protocol on the phantom, all individual sensitivity images were integrated to render a combined impedance map defined as:

$$\overline{\Delta Ve}(n,m,p) = \|\overrightarrow{Ve}_{n,m,p} - \overrightarrow{Ve}_{ref}\|$$
$$\forall \; n = 1{:}Ni, m = 1{:}Nj, p = 1{:}Nl$$

As a result, the combined sensitivity $\overline{\Delta Ve}(n,m,p)$ represents the norm of the voltage difference under all current sources and voltage measurements for an impedance variation at location (n,m,p). Similarly, impedance selectivity of the integrated images was also calculated according to:

$$\overline{\Delta Ve}_{sel}(n,m,p) = \left\| \vec{Ve}_{n,m,p} - \vec{Ve}_{i,j,l} \right\|$$

$$\forall\, n = 1:Ni,\, m = 1:Nj,\, p = 1:Nl$$

This analysis measured the difference of voltage change for an impedance change at a voxel (n,m,p) relative to all other voxels. Together, these master maps served as the templates to calculate regional sensitivity and selectivity of EIT under various parametric variations, phantom aberrations, or hardware imperfections. With color-scaling, they allowed for graphical identification of areas having the highest detection resolution and detectability.

D. Parametric Optimization Studies

To demonstrate versatility, both individual and integrated impedance sensitivity maps were calculated and rendered for phantoms with both uniform and non-uniform distribution of features. The non-uniform features tested took the form of user-defined shapes, sizes, and electrical properties such as voxel impedance, and different locations in the phantom. These case studies examined the current and voltage distribution over a series of expected (uniform) and intentional (non-uniform) scenarios in which the impedance sensitivity map must hold true. Therefore, these parametric adjustment investigations are idyllic to serve as calibration mechanism for the testing of new EIT parameters, phantom features, hardware implementation, and etc. In this report, we selected the following two cases to demonstrate: 1) the effect of phantom feature location has on overall EIT sensitivity; and 2) a comparison between two common stimulation and measurement protocols, namely the Neighboring Method and the Opposite Method.

III. SIMULATION RESULTS

For a given phantom of varying degrees of feature homogeneity, complexity, and density, the ability to track the behavior of the injected current and measured voltage reflective of the phantom feature influence greatly aids in the evaluation of EIT sensing performance. We selected a 20-electrode set to generate a reasonable visualization. However, any number of electrodes can be implemented. And as the electrode number increased, the distance between each electrode automatically decreased, leading to lower voltages as the measurement electrodes became closer to the current electrodes. The grid size of our phantom was fixed throughout the study. However, it is a programmable parameter in which the denser the grid size can contribute to an increase in effective spacing between the electrodes, reflected as an increase in resolution that enhances the voltage drops.

Figure 4 displays an instantaneous image of the voltage and current distribution at a fixed current stimulation location. It's a snapshot of a full, dynamic visualization that follows the movement of the electrode rotation sequence as the EIT sensor operates in a counterclockwise direction. The node voltage of each voxel is intensity-mapped and displayed for intuitive

readout of the voltage variation as a result of the phantom features within. The magnitude of the current is represented by the size of the arrows as they travel diffusively across all voxels. Current magnitude is greatest in regions with lowest conductivity between the source and sink electrode, and weakest as the current moves further away or run into features of large impedance. This behavior can be better visualized in a 2D plane as illustrated in Figure 4c-d.
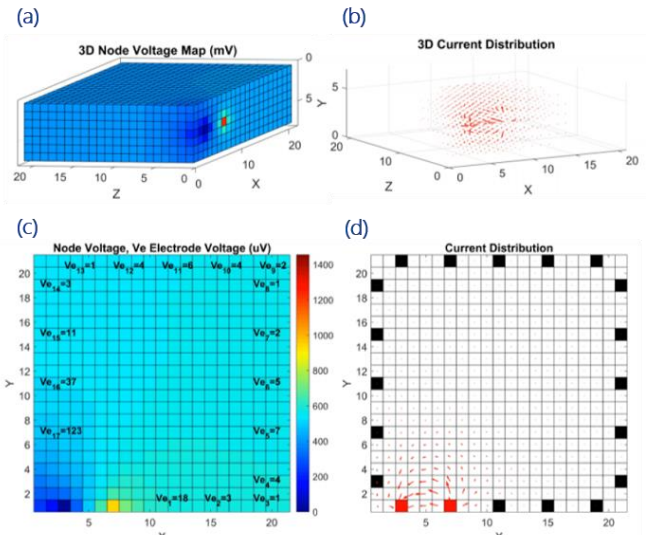

Figure 4. (a) 3D Node voltage and (b) injected current distribution in a non-uniform phantom. (c) 2D top view of the differential voltage and (d) current distribution of neighboring pair of electrodes. Arrow size indicates magnitude as it passes through each voxel.

The four tissue types illustrated in Figure 2 are incorporated in this simulation but not shown in Figure 4. However, instantaneous analysis of these distribution maps was able to show altered current paths due to the increased impedance from the fat tissue, or increased voltage drop due to closer proximity of the electrodes to arteries or muscles.

A. Sensitivity & Specificity Performance

Impedance map of the phantom image had been calculated individually ($\overline{\Delta Ve}_{k,s}$) for each current stimulation location k and its full frame of voltage measurement s. The result is an impedance distribution with magnitude intensity color-coded to demonstrate stepwise tracking of variations within the phantom during EIT operation. This is illustrated by Figure 5 where nine selected combination of stimulation and measurement pairs are represented. The added dash-lines highlights the paths of greatest impedance perturbation or sensitivity between the electrode pairs. It is evident that when the measurement electrodes were closest to the injected current electrodes, highest zones of sensitivity occurred near or between the respective electrodes due to the dense current flux. And lowest sensitivity results when they were furthest away (e.g. $\overline{\Delta Ve}_{5,10}$). These sensitivity paths were also affected by the features (of varying impedances, shapes, sizes, etc.) in between the stimulation and measurement electrode pairs.

Individual sensitivity map is advantageous in the stepwise analysis of the EIT sensing process. Conversely, an integrated map presents a collective, practical assessment of the phantom's sensitivity to EIT's bioelectrical interrogation. As
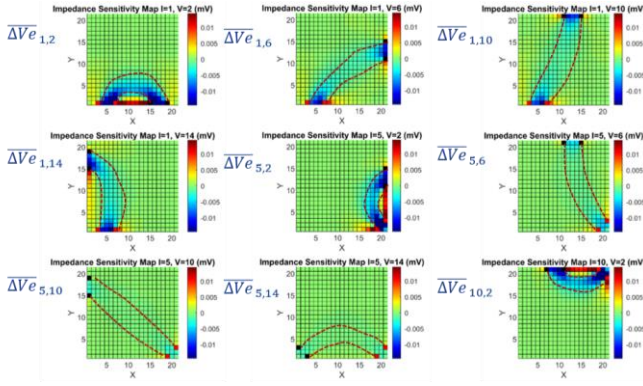
Figure 5. Selected 2D individual impedance sensitivity images for various current stimulation electrode pair locations k in $(Ve_{k,s})$. And voltage measurement location s. Dotted lines highlight the connectivity of impedance in relation to current to voltage electrode pair positions.

shown in Figure 6a, for a given square phantom, the resultant outcome of evaluating each pixel's sensitivity to an impedance perturbation can be summarized in one ultimate combined image. This map intuitively highlights the most and least favorable regions for detecting the greatest changes under the prescribed EIT protocol. Not surprisingly, for a square phantom, sharp corners presented the densest current flux, hence the highest sensitivity as indicated by green-yellow gradient. Second highest regions can be found near the electrode-phantom interface. Due to the diffusive nature of applied electric current, the Neighboring stimulation method produced weak depth penetration, which is a characteristic consistent with wide literature reports. However, this sensitivity map demonstrated a gradient, progressive transition from strong to weak spots in the phantom features. Furthermore, a combined selectivity map was also calculated and produced as shown in Figure 6b to accompany the sensitivity map. It is particularly advantageous in showing feature distinction during multiple simultaneous impedance changes occurring in the phantom. Hence, knowledge pertaining to how selective an area is on the phantom to EIT detection can be visually ascertained.
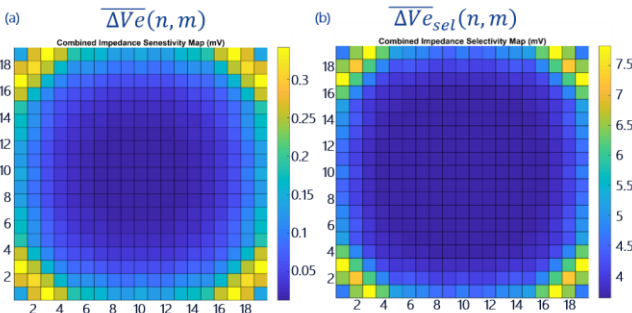

Figure 6. (a) Combined Impedance sensitivity image $\overline{\Delta Ve}(n,m)$ and (b) impedance selectivity image $\overline{\Delta Ve_{sel}}(n,m)$ for a uniform phantom without any internal features under the neighboring stimulation and measurement protocol.

B. Uniform vs Non-Uniform Phantoms

There are many advantages to employing uniform or simplified phantom at the lower expense of computation complexity and speed. In our simulation, phantom of uniform feature served to validate the expected operation and performance outcome of the EIT under set parameters. The 2D

referenced phantom feature layout in Figure 7a was subjected to both individual and integrated sensitivity and selectivity analysis in our simulation. The combined outcome is shown in Figure 7b in 2D for clarity (selectivity map is not shown). The overall impedance is lowered compared to that of the uniform phantom to account for the reduced conductivities of the features. Tissue contrast plays a key role in creating distinguishable features on the simulation. The subcutaneous fat for an instance surrounded other tissues and carried a relative low conductance of 0.04 mho/m. When the stimulating current reached the highly conductive muscle tissues (0.3 mho/m), a drop in tissue impedance aided in the sharp transition from a low current to a higher current flow, hence, producing a contrast at their interfacial boundary. The same distinction can be made with the arteries which also had a conductance (0.7 mho/m) higher than that of the fat tissue. Even with relatively small dimensions, the feature contrast was clear.
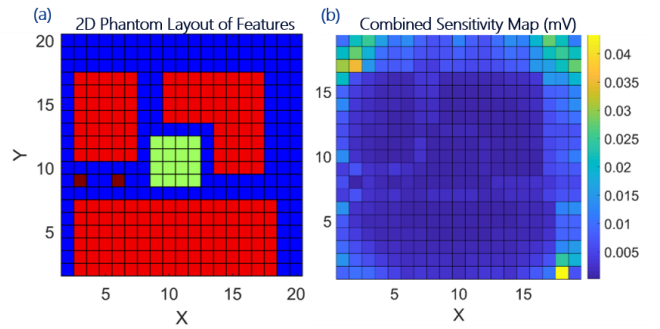

Figure 7. (a) Phantom feature as conductivity layouts in 2D showing 4 types of tissues. Intensity bar not shown, refer to figure 2b. (b) Simulated combined sensitivity image on the phantom feature shown in (a).

However, tissue depth became the limiting factor (under the Neighboring method) for all the tissue types. The bone being the innermost tissue possessed the weakest sensitivity, yet with the provision of a tissue contrast such as that provided by the connective fat, edges of the bone, oddly-shaped muscles, small-sized arteries that extended further in depth can still be calculated and visually identified. This finding showed that importance of having the right tool to elucidate the bioelectrical interactions between tissues can lead to better understanding and new implementation.

C. Parametric Evaluations

A myriad of variables influences the sensitivity of EIT. To identify and evaluate these variables and their contribution to sensor performance, a series of experiments were performed using our simulation platform. Under a more analytical setting, we varied the location of a single object within a uniform phantom under the same EIT protocol as described so far and evaluated how its location in relation to the electrodes contribute to the sensitivity outcome. Figure 8a shows a 40-electrode set around a 40 by 40 grid with their location numerically marked on all sides. As the blue square object moved toward location 25 (upper edge), voltage measurements from all electrodes at all object locations were plotted simultaneously (Figure 8b) to track any signs of voltage deviation. As highlighted by the blue box in the figure, selective locations of the objects toward the upper
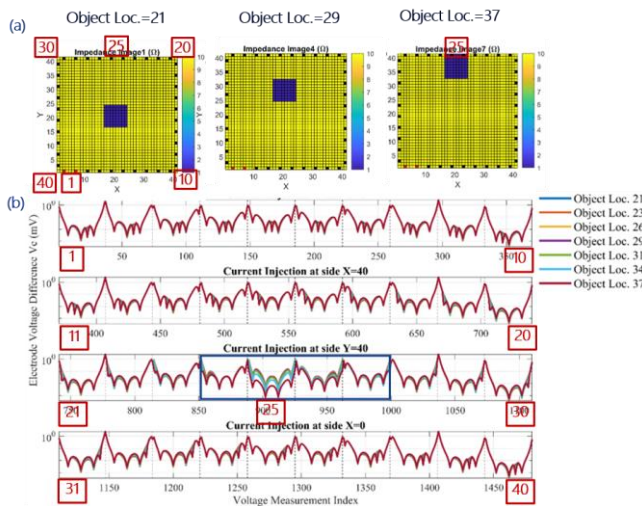
Figure 8. (a) Reference image $R(i,j)_{ref}$ showing a square feature of fixed size but varying in location (towards the upper edge) in the phantom. Each feature has a 10% lower relative impedance from the background (yellow). (b) Differential voltage measurement for this reference image at different locations around the phantom during current injection (indicated by different color solid lines).

edge rendered proportional increases in differential voltage measured by the rotating surface electrodes. As a result, both EIT sensitivity and selectivity increased exponentially as the object move closer towards the electrodes (Figure 9). This is true for different stimulation and measurement protocols that we tested. Other similar experiments concerning the effects of the object/feature geometry, dimension, number, and electrical property have been equally illuminating but not discussed in this report.
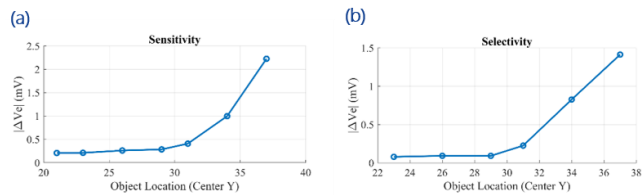
$$\Delta Ve_i = \left\| \vec{Ve_i} - \vec{Ve}_{ref} \right\|$$

$$\Delta Ve_i = \left\| \vec{Ve_i} - \vec{Ve}_{i-1} \right\|$$

Figure 9. (a) Sensitivity and (b) selectivity of the experiment in Figure 9 as a function of object changing locations.

Two popular stimulation and measurement protocols are the Neighboring and Opposite method. They are conversely related to each other and can provide subjective insights about the phantom features. To evaluate their contribution to sensitivity, we subjected the referenced phantom (Figure 2) to these two modes of EIT operation, and the combined sensitivity maps are shown in Figure 10a-b. Their intensity values were normalized with respect to the maximum intensity value of each map, allowing better comparison of the center sensitivity of the Opposite mode relative to the Neighboring mode. The current distribution maps in Figure 10c-d illustrates the current paths in which these two protocols undertook to navigate around the complex features and interact under their geographical and electrical influences. The magnitude of current paths visualized by

arrow sizes were reflective of their interactions with the four tissue types. The Opposite Method functions to inject current through the depth of the phantom, and hence capable of providing more contrast and clarity to the features in between. As demonstrated by the comparison 2D sensitivity maps in the figure, boundaries between the fat and other lower conductance tissues became more identifiable. Selective regions between these two sensitivity maps were used to calculate the exact improvement. At the center, our simulation showed for this specific phantom, just changing the protocol alone can improve EIT sensitivity by 36%. This simulation tool can easily accommodate other stimulation and measurement protocols such as the adaptive or cross pattern.
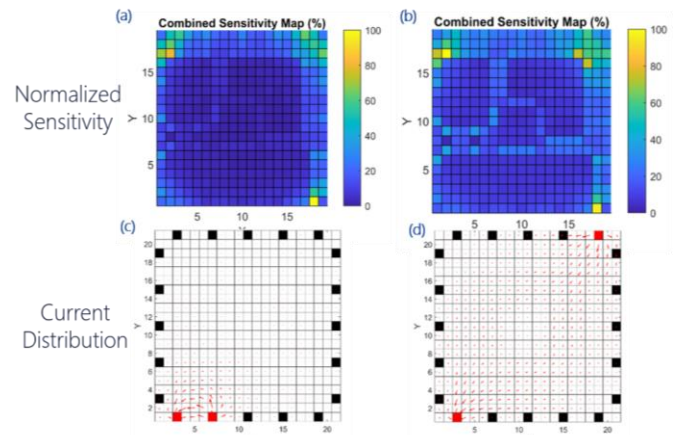

Figure 10. Combined sensitivity image with normalized values for the non-uniform phantom under (a) Neighboring and (b) Opposite stimulation and measurement protocol. (c) and (d) shows their corresponding current distribution on the inner features of the phantom.

IV. CONCLUSION

We presented a bioelectrical simulation platform for the performance evaluation, and parametric optimization of the EIT sensor using a non-finite element model-based analysis approach. Adapting the complete cell equivalent circuit model to build larger and more complex tissues and organ systems, we demonstrate a physiologically relevant platform capable of producing prediction based on real-life bioelectrical interactions in the body. Thus, allowing 1) more accurate estimation by EIT sensors in general; and 2) dynamic processes such as pulsatile blood vessels or beating heart and other transient physiological processes to be modeled simply and accurately; and 3) tailored design and tuning of the EIT sensor for specific biologic targets. Utilizing this bioelectrical platform, we constructed a new set of sensitivity and selectivity algorithms to visually inspect parameters and variables that contribute to EIT's sensing strengths and weakness without influence of image reconstruction algorithms. With the option of performing stepwise or comprehensive simulation on a programmable bioelectrical phantom, we bring forth a more accurate and illuminating EIT simulation tool capable of predicting the performance of the sensor under desired modes of operation, parameters of function, and variables of experimentation for the diverse purpose of EIT applications.

REFERENCES

[1]   A. M. Luks and E. R. Swenson, "Pulse oximetry for monitoring patients with COVID-19 at home potential pitfalls and practical guidance," *Annals of the American Thoracic Society*, vol. 17, no. 9. American Thoracic Society, pp. 1040–1046, Sep. 01, 2020, doi: 10.1513/AnnalsATS.202005-418FR.

[2]   A. Adler and A. Boyle, "Electrical Impedance Tomography," in *Wiley Encyclopedia of Electrical and Electronics Engineering*, Wiley, 2019, pp. 1–16.

[3]   L. Tarassenko and P. Rolfe, "Imaging spatial distributions of resistivity—an alternative approach," *Electron. Lett.*, vol. 20, no. 14, pp. 574–576, Jul. 1984, doi: 10.1049/el:19840397.

[4]   A. Adler, Y. Berthiaume, R. Guardo, and R. Amyot, "Imaging of pulmonary edema with electrical impedance tomography," in *Annual International Conference of the IEEE Engineering in Medicine and Biology - Proceedings*, 1995, vol. 17, no. 1, pp. 557–558, doi: 10.1109/iembs.1995.575248.

[5]   N. D. Harris, A. J. Suggett, D. C. Barber, and B. H. Brown, "Applications of applied potential tomography (APT) in respiratory medicine," *Clin. Phys. Physiol. Meas.*, vol. 8, no. 4A, pp. 155–165, Nov. 1987, doi: 10.1088/0143-0815/8/4A/020.

[6]   T. Meier *et al.*, "Assessment of regional lung recruitment and derecruitment during a PEEP trial based on electrical impedance tomography," *Intensive Care Med.*, vol. 34, no. 3, pp. 543–550, Mar. 2008, doi: 10.1007/s00134-007-0786-9.

[7]   J. Conway, "Electrical impedance tomography for thermal monitoring of hyperthermia treatment: An assessment using in vitro and in vivo measurements," *Clin. Phys. Physiol. Meas.*, vol. 8, no. 4A, pp. 141–146, Nov. 1987, doi: 10.1088/0143-0815/8/4A/018.

[8]   T. M. T. Pham, M. Yuill, C. Dakin, and A. Schibler, "Regional ventilation distribution in the first 6 months of life," *Eur. Respir. J.*, vol. 37, no. 4, pp. 919–924, Apr. 2011, doi: 10.1183/09031936.00034310.

[9]   © S Prasad, D. Houserkova, J. Campbell, S. Prasad, D. Houserkova, and J. Campbell, "BREAST IMAGING USING 3D ELECTRICAL IMPEDENCE TOMOGRAPHY," 2008.

[10]   S. Hannan, M. Faulkner, K. Aristovich, J. Avery, M. Walker, and D. Holder, "Imaging fast electrical activity in the brain during ictal epileptiform discharges with electrical impedance tomography," *NeuroImage Clin.*, vol. 20, pp. 674–684, Jan. 2018, doi: 10.1016/j.nicl.2018.09.004.

[11]   P. Linderholm, L. Marescot, M. H. Loke, and P. Renaud, "Cell culture imaging using microimpedance tomography," *IEEE Trans. Biomed. Eng.*, vol. 55, no. 1, pp. 138–146, Jan. 2008, doi: 10.1109/TBME.2007.910649.

[12]   T. Sun, S. Tsuda, N. G. Green, K. P. Zauner, and H. Morgan, *ON-CHIP ELECTRICAL IMPEDANCE TOMOGRAPHY FOR MONIROTING THE KINETICS IN THE CELL CULTURE.* .

[13]   E. Ravagli, S. Mastitskaya, N. Thompson, K. Aristovich, and D. Holder, "Optimization of the electrode drive pattern for imaging fascicular compound action potentials in peripheral nerve with fast neural electrical impedance tomography," *Physiol. Meas.*, vol. 40, no. 11, p. 115007, Dec. 2019, doi: 10.1088/1361-6579/ab54eb.

[14]   J. Avery, T. Dowrick, M. Faulkner, N. Goren, and D. Holder, "A Versatile and Reproducible Multi-Frequency Electrical Impedance Tomography System," *Sensors*, vol. 17, no. 2, p. 280, Jan. 2017, doi: 10.3390/s17020280.

[15]   S. Hong *et al.*, "A 4.9 mΩ-sensitivity mobile electrical impedance tomography IC for early breast-cancer detection system," *IEEE J. Solid-State Circuits*, vol. 50, no. 1, pp. 245–257, Jan. 2015, doi: 10.1109/JSSC.2014.2355835.

[16]   K. G. Boone and D. S. Holder, "Current approaches to analogue instrumentation design in electrical impedance tomography," *Physiological Measurement*, vol. 17, no. 4. IOP Publishing, pp. 229–247, Nov. 01, 1996, doi: 10.1088/0967-3334/17/4/001.

[17]   W. R. B. Lionheart, "EIT reconstruction algorithms: Pitfalls, challenges and recent developments," in *Physiological Measurement*, Feb. 2004, vol. 25, no. 1, pp. 125–142, doi: 10.1088/0967-3334/25/1/021.

[18]   A. Adler, B. Grychtol, and R. Bayford, "Why is EIT so hard, and what are we doing about it?," *Physiological Measurement*, vol. 36, no. 6. Institute of Physics Publishing, pp. 1067–1073, Jun. 01, 2015, doi: 10.1088/0967-3334/36/6/1067.

[19]   M. Vauhkonen, et al., "A matlab package for the EIDORS project to reconstruct two-dimensional EIT images," *Physiol. Meas.*, vol. 22, no. 1, p. 107, 2001.

[20]   N. Polydorides and W. R. B. Lionheart, "A Matlab toolkit for three-dimensional electrical impedance tomography: A contribution to the Electrical Impedance and Diffuse Optical Reconstruction Software project," *Meas. Sci. Technol.*, vol. 13, no. 12, pp. 1871–1883, Nov. 2002, doi: 10.1088/0957-0233/13/12/310.

[21]   S. Gabriel, R. W. Lau, and C. Gabriel, *The dielectric properties of biological tissues: III. Parametric models for the dielectric spectrum of tissues*, vol. 41, no. 11. Phys Med Biol, 1996.

[22]   B. Ibrahim, D. A. Hall, and R. Jafari, "Bio-impedance Simulation Platform using 3D Time-Varying Impedance Grid for Arterial Pulse Wave Modeling," Oct. 2019, doi: 10.1109/BIOCAS.2019.8919198.